Brief communication: Impact of mesh resolution for MISMIP and MISMIP3d experiments using Elmer/Ice. Supplementary material.

O. Gagliardini, J. Brondex, F. Gillet-Chaulet, L. Tavard,
V. Peyaud and G. Durand

January 7, 2016

1 Possible implementations of a discontinuous friction at the GL

Elmer/Ice uses the finite element method and, by construction, all the field variables are defined as nodal values and so is the GL which follows the edges of the elements. The GL dynamics is solved as a contact problem between the ice and the underlying bed. The effectiveness of the contact is tested for each node belonging on the bed by comparing the residual force of the Stokes equations to the force exerted by the sea water pressure (for more details, see Durand et al., 2009a). By definition, the GL is the ensemble of nodes which are the last in contact with the bedrock, i.e. for which the Stokes residual is strickly larger than the water force. Furthermore, the GL marks the transition between ice in contact with the bedrock, and therefore subject to friction, and ice in contact with the ocean with a free slip condition.

In the case of a discontinuous friction at the GL, three modelling strategies can be used to impose this transition at the GL between the slip condition to the free-slip condition (see Fig. S1). The first strategy is assuming that the GL defines the last grounded (LG) nodes and that friction is applied up to the nodes belonging to the GL. In the second, the nodes belonging to the GL are assumed to be the first floating (FF) nodes and are already freely slipping. The third strategy assumes that the friction is discontinuous (DI) at the nodes belonging to the GL: friction at these nodes is only applied if integrating over an element where all other nodes are also in contact with the bedrock but a free slip condition is applied if the node belongs to an element where at least one node is in contact with the ocean.

The three implementation strategies are illustrated in a two-dimensional flow line configuration in Fig. S1.

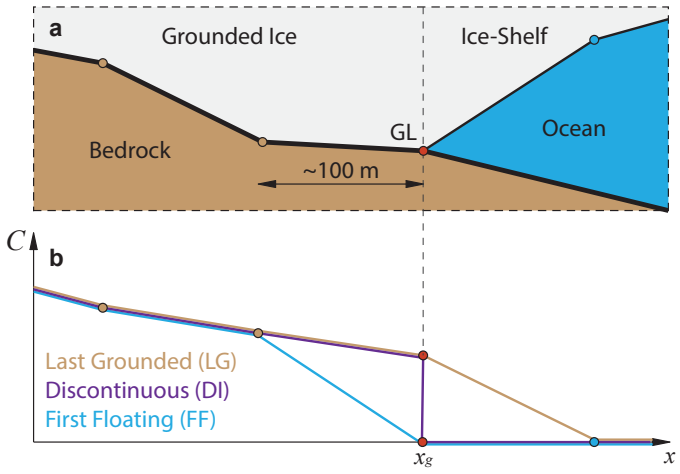

Figure S1: Two-dimensional schematic explanation of the three different implementations to impose the friction in the close vicinity of the GL. **(a)** Zoom on the triple junction point between ice, bedrock and ocean, defined as the GL (red dot and x_g) and **(b)** changes in the friction parameter C close to the GL, with the three methods: friction is applied at the GL which is then the last grounded node (LG, brown), pure sliding is applied at the GL which is then the first floating node (FF, blue) and the friction is discontinuous at the GL (DI, purple). The coloured dots are the bottom boundary nodes of the finite element mesh: brown in contact with the bedrock, blue in contact with the ocean and red at the GL.

To build the finite element system to be solved, the friction needs to be interpolated at the integration points of each element. For the LG implementation, the first elements in contact with the ocean are therefore undergoing some friction due to the interpolation between a non-zero friction value at the nodes belonging to the GL and zero value at the other nodes. On the contrary, for the FF implementation the friction is lowered in the last elements in contact with the bedrock because of the vanishing friction at the GL nodes. The DI implementation is therefore certainly the most physical as friction is applied up to the GL but switched off in the first elements in contact with ocean. However the three methods should converge to the same solution when the elements size decreases. Moreover, the three methods give identical results if the friction at the GL is null, whatever the mesh discretisation. Up to now, all the published Elmer/Ice results were obtained using the LG method (Durand et al., 2009a,b, 2011; Gagliardini et al., 2010, 2013; Favier et al., 2012, 2014; Drouet et al., 2013; Gudmundsson et al., 2012; Pattyn et al., 2012, 2013; Krug et al., 2014).

2 New results for MISMIP3d P75D

The three implementations are compared using the diagnostic experiment P75D of MISMIP3d. The objective of experiment P75D was to compare the velocity field obtained by the various Stokes approximations for a prescribed glacier geometry. This geometry, the same for all numerical models, was defined as the one obtained with Elmer/Ice at $t = 100$ a for experiment P75S (the last time step of the perturbation experiment, see main text and Pattyn et al. (2013) for more details on the experimental setups). We recall that at that time this geometry was obtained using the LG implementation. Exactly the same mesh as in Pattyn et al. (2013) is used here to compare the three methods on this diagnostic experiment.

In Pattyn et al. (2013), the boundary condition (BC) applied at the base of the ice-shelf for the diagnostic experiment was not specified. If this condition is clear for lower-order Stokes models (i.e. for vertically integrated models), this is not the case when solving for the full-Stokes solution. We first enumerate the possible BCs to be applied at the base of an ice-shelf for a Stokes model. The velocity field obtained with the three methods for interpolating the friction at the GL are then compared.

For a Stokes *prognostic* simulation, assuming no accretion/melting, Durand et al. (2009a) have shown that the following BC should be applied at the base of the ice-shelf (BC1):

$$\sigma_{\mathrm{nn}}|_{\mathrm{b}} = -\rho_{\mathrm{w}} g (l_{\mathrm{w}} - z_{\mathrm{b}}) + C_{\mathrm{n}} u_{\mathrm{n}}, \tag{1}$$

where $\sigma_{\mathrm{nn}}|_{\mathrm{b}}$ is the normal Cauchy stress applied at the base of the ice-shelf, l_{w} and z_{b} are the sea and ice-shelf bottom elevations, respectively, ρ_{w} the water density, g the gravity, $u_{\mathrm{n}} = \vec{u} \cdot \vec{n}$ the normal component of the ice velocity and $C_{\mathrm{n}} = \rho_{\mathrm{w}} g \sqrt{1 + (\partial z_{\mathrm{b}}/\partial x)^2 + (\partial z_{\mathrm{b}}/\partial y)^2} \mathrm{d}t$. As explained in Durand et al. (2009a), C_{n} acts like a damper on the bottom interface so that the normal stress induced by $C_{\mathrm{n}} u_{\mathrm{n}}$ will counteract the buoyancy stress and will avoid too large velocity that would arise even for a small buoyancy disequilibrium.

For a Stokes *diagnostic* simulation, one can think about two other BC for the ocean/ice interface. For all of them we implicitly assume that there is no melting or marine ice accretion below the ice-shelf.

The first is deduced from the free surface evolution assuming a steady-state geometry and no melting or accretion. Under such hypotheses, the bottom free surface evolution reduces to the simple Dirichlet BC (BC2):

$$u_{\mathrm{n}} = \vec{u} \cdot \vec{n} = 0. \tag{2}$$

The second, a Neumann BC, assumes the buoyancy equilibrium at the interface ice/ocean (BC3):

$$\sigma_{\mathrm{nn}}|_{\mathrm{b}} = -\rho_{\mathrm{w}} g (l_{\mathrm{w}} - z_{\mathrm{b}}). \tag{3}$$

BC1 derives from BC3 with an implicit evaluation of z_b at $t + \mathrm{d}t$ using the free surface equation for z_b. Note that vertically integrated models does not require any BC at the base of the ice-shelf for a diagnostic simulation as far as the vertical velocity is not computed.

For a steady-state geometry and assuming no melting or accretion below the ice-shelf, all three BC should give the same velocity field as one expects $u_\mathrm{n} = 0$ and the buoyancy equilibrium to be fulfilled. Here, for the diagnostic experiment P75D, because the geometry does correspond to a snapshot of a transient evolution, the ice-shelf is not exactly at the buoyancy equilibrium. This is true for the LG method with which the geometry was obtained, and even worse for the two other methods which have completely different geometries after the 100 year perturbation (see discussion below and Fig. S4). We therefore tested the three possibilities for the bottom ice-shelf BC.

Even for the LG method, no convergence of the non-linear iteration was obtained with the Neumann BC3. This indicates that even a small buoyancy disequilibrium renders the Stokes problem ill-posed. Adding the viscous damper C_n to the hydrostatic stress (BC1 given by Eq. 1) has a stabilisation effect and allow convergence. No results are therefore presented for BC3. Results for the two other BCs, BC1 and BC2, are presented below.

Changes along the x direction of the x component of the surface velocity at $y = 0$ (symmetry axis for the flow and centre for the perturbation of the basal friction parameter) and at $y = 50\,\mathrm{km}$ (side of the domain) are presented for all three implementation strategies and for the two BCs BC1 and BC2 in Fig. S2. As can be seen in this figure, the LG method leads to the smallest velocity and the FF method to the largest, while the velocity obtained with the DI method is between the two. The way the friction is interpolated at the GL not only influences the velocity downstream from the GL but also over a few ice thicknesses upstream from the GL. At the GL, the relative difference in velocity between LG and FF methods is as high as 23 % for $y = 0$ and 17 % for $y = 50\,\mathrm{km}$. The difference is greater at $y = 0$ than at $y = 50\,\mathrm{km}$ despite less friction at the GL at $y = 0$ than at $y = 50\,\mathrm{km}$. As the vertical gradients of horizontal velocity are small at the GL, similar differences would be expected in ice fluxes trough the GL. As depicted in Fig. S3, these differences in velocity are induced by different distributions of the basal shear stress between the three methods. Figure S3 shows high relative differences of the local tangential stress between the three methods (larger than 50% at some place), but these differences are located in the close vicinity of the GL and they compensate when integrated over all the bedrock. Indeed, all three methods have the same total traction force at the base, as required by the global equilibrium of the ice mass submitted to the gravity force. As expected, the basal shear stress is overestimated downstream the GL for the LG method relative to the

DI method (Fig. S3**a**). This excess of stress downstream the GL for the LG method is compensated by a lower shear stress upstream the GL. The opposite pattern is observed for the FF method relative to the DI method (Fig. S3**b**). If the change in basal stress stays local, the induced changes on the velocity are transported and cumulated downstream, explaining the shape of the curves depicted in Fig. S2. Given the mesh resolution adopted to produce these results, the way the friction law is applied in the very close vicinity of the GL is found to have a significant effect on the velocity field.

The Elmer/Ice velocity solution for experiment P75D in Pattyn et al. (2013) is also shown in Fig. S2 (black curve, named LFA in Pattyn et al., 2013). As Elmer/Ice has been used to design the experiment, the geometry and velocity field were directly extracted from the last time step of the transient experiment P75S. Because of the time-integration scheme in Elmer/Ice, the velocity field was in fact computed from the previous time step geometry ($t - 0.5\,\mathrm{a}$), and not computed as the steady-state solution of the geometry provided. This explains the minor difference between the published velocity solution and the newly computed LG solution (brown thick curve in Fig. S2).

The two solutions for the BC below the ice-shelf give slightly different results for all three methods. As shown in Fig. S2, the horizontal flow at the GL for BC2 is found to be slower by approximately 1 % than the one for BC1, for all three methods and both at $y = 0$ and $y = 50\,\mathrm{km}$. For BC1, despite its theoretical validity only for transient simulation (time step $\mathrm{d}t$ entering Eq. 1), the results presented in Fig. S2 were obtained assuming an arbitrary time step $\mathrm{d}t = 1\,\mathrm{a}$. Anyway, other realistic choices of $\mathrm{d}t$ would not change significantly the results as the term $C_\mathrm{n} u_\mathrm{n}$ in Eq. (1) is found to be at least 10^3 times smaller than the hydrostatic pressure $-\rho_\mathrm{w} g(l_\mathrm{w} - z_\mathrm{b})$. Because the Dirichlet boundary condition BC2 is certainly the easiest to implement and test, the results for both BCs BC1 and BC2 are given as Supplement. For future comparisons, it would be therefore more consistent to use the results in the Supplement of the present publication, either with the buoyancy BC1 or the Dirichlet BC2 applied at the base of the ice-shelf.

2.1 Complementary Figures and Table for experiments MISMIP3d P75S and P75R

Figure S4 shows the evolution of the GL during the 100 years of the perturbation (from 0 to 100 years) and during the same time after the perturbation has been removed (from 100 to 0 years), at $y = 0$ and $y = 50\,\mathrm{km}$. As shown in this figure, the transient responses of the three methods relative to their initial position x_{G_0} are similar during the first 5 years, but then differ significantly. Interestingly, if the

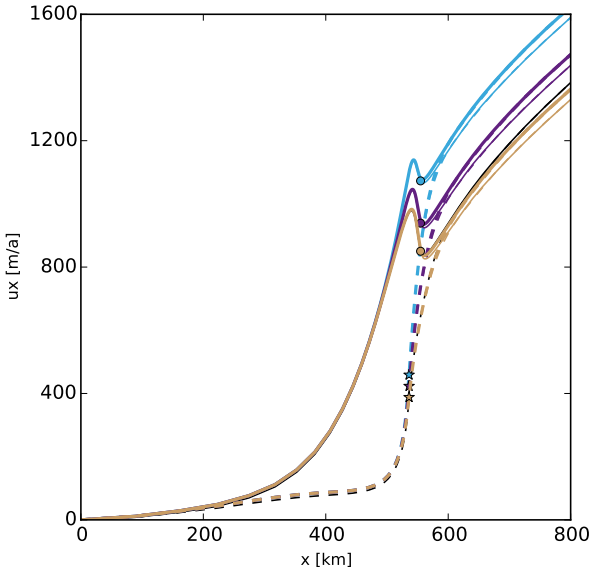

Figure S2: Experiment MISMIP3d P75D: surface velocity along the x direction for the three different methods: LG (brown), DI (purple) and FF (blue) on the symmetry axis ($y = 0$; continuous line) and on the free-slip boundary ($y = 50\,\mathrm{km}$, dashed line), for BC (Eq. 1) (thick line) and BC (Eq. 2) (thin line). The LFA Elmer/Ice solution published in Pattyn et al. (2013) is represented in black (mostly hidden by the LG brown thick curve), The signs indicate the GL position in $y = 0$ (dot) and $y = 50\,\mathrm{km}$ (star).

LG GL is continuously advancing at $y = 0$, this is not anymore the case for the two other methods. The rapid advance of the FF GL position at $y = 0$ occurring during the first years is then followed by a retreat of almost the same magnitude after 100 years, with a difference lower than 2 km with the initial GL position, when it is almost 19 km for the LG one (see Table S1). After the perturbation is removed, the GL starts to move back towards its initial steady state position. Nevertheless, after 100 years (dashed lines from 100 to 0 a in Fig. S4), the GLs are still far from having reached again the steady state position ($\Delta_{x_G} = 0$). The LG method is the fastest in coming back to its steady state position whereas the FF is the slowest. These results were obtained for a resolution of $N_y = 20$ elements in the lateral direction. Figures S5 and S6 present the results for lateral resolutions of $N_y = 40$ and $N_y = 80$, respectively, everything else being the same. These new results are discussed in the main paper.

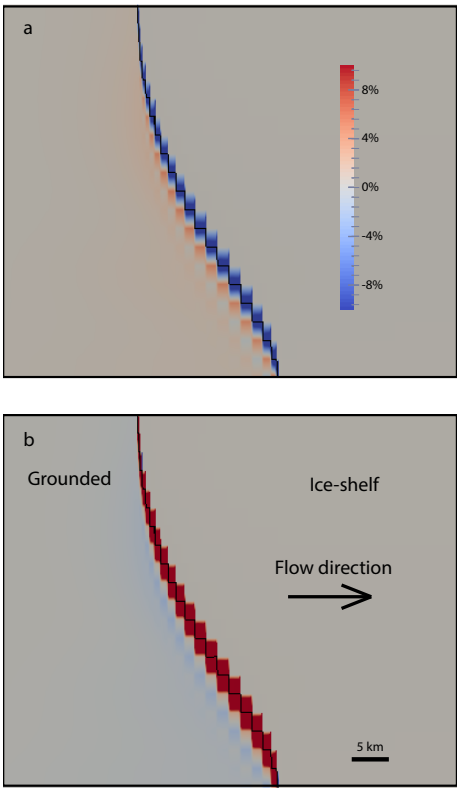

Figure S3: Experiment MISMIP3d P75D: relative difference between the shear stress at the bed for **(a)** the DI and LG methods and **(b)** the DI and FF methods [%]. The black line indicates the GL position. The tangent used to compute the shear stress is the one perpendicular to the transverse direction of the flow.

Table S1: Experiment MISMIP3d P75S and P75R: initial steady GL position (x_{G_0}, km) and differences between the final ($t = 100$ a) and initial GL positions (Δx_G, km) in $y = 0$ and $y = 50\,\mathrm{km}$, as a function of the method and the number of element along the y direction (N_y). LFA is the Elmer/Ice solution published in Pattyn et al. (2013).

	Last Grounded LG			Discontinuous DI			First Floating FF			LFA
N_y	20	40	80	20	40	80	20	40	80	20
x_{G_0}		529.550			526.800			522.350		537.078
$\Delta x_G\|_0$	18.950	16.350	15.050	9.250	10.825	11.950	1.950	6.425	9.900	17.622
$\Delta x_G\|_{50}$	−0.100	−2.750	−3.850	−8.000	−7.050	−6.250	−13.050	−10.250	−7.850	−1.178

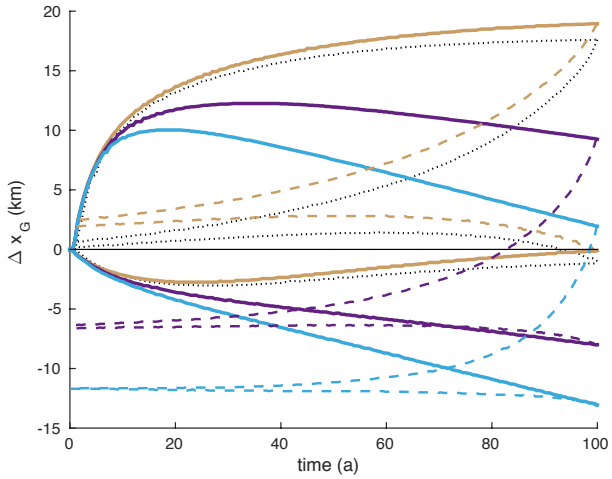

Figure S4: Experiment MISMIP3d P75S and P75R: time-dependent plot of the GL position relative to the steady position x_{G_0} (see Table S1) during (P75S; continuous) and after (P75R; dashed) the basal sliding perturbation, on the symmetry axis ($y = 0$; top curves) and on the free-slip boundary ($y = 50\,\mathrm{km}$; bottom curves) for the three different implementations: LG (brown), DI (purple) and FF (blue). The black dotted curve is the GL evolution for the LFA solution published in Pattyn et al. (2013) (LG method and $N_y = 20$). The mesh resolution in the y direction is $N_y = 20$ elements for all simulations.

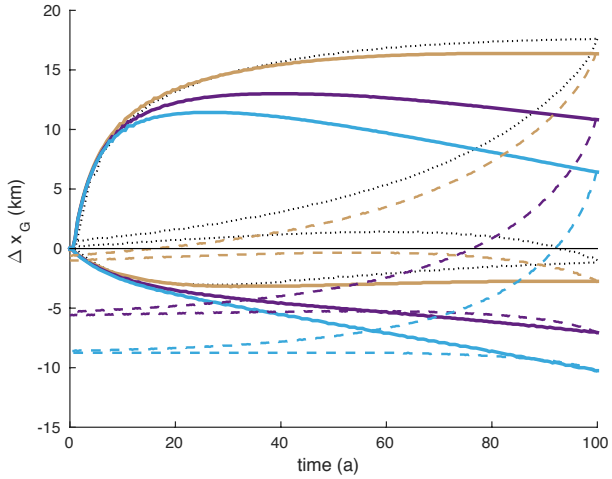

Figure S5: Same as Fig. S4 but for a lateral discretisation of $N_y = 40$ elements.

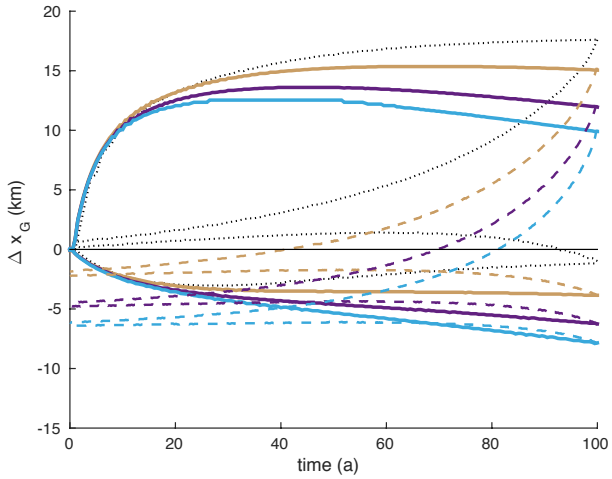

Figure S6: Same as Fig. S4 but for a lateral discretisation of $N_y = 80$ elements.

References

Drouet, A.-S., Docquier, D., Durand, G., Hindmarsh, R., Pattyn, F., Gagliardini, O., and Zwinger, T.: Grounding line transient response in marine ice sheet models, The Cryosphere, 7, 395–406, 2013.

Durand, G., Gagliardini, O., de Fleurian, B., Zwinger, T., and Le Meur, E.: Marine ice sheet dynamics: Hysteresis and neutral equilibrium, J. Geophys. Res. (Earth Surface), 114, F03 009, doi:doi:10.1029/2008JF001170, 2009a.

Durand, G., Gagliardini, O., Zwinger, T., Le Meur, E., and Hindmarsh, R. C. A.: Full-Stokes modeling of marine ice-sheets: influence of the grid size, Annals of Glaciology, 52, 109–114, doi:doi:10.3189/172756409789624283, 2009b.

Durand, G., Gagliardini, O., Favier, L., Zwinger, T., and Le Meur, E.: Impact of bedrock description on modeling ice sheet dynamics, Geophysical Research Letters, 38, L20 501, doi:doi:10.1029/2011GL048892, 2011.

Favier, L., Gagliardini, O., Durand, G., and Zwinger, T.: A three-dimensional full Stokes model of the grounding line dynamics: effect of a pinning point beneath the ice shelf, The Cryosphere, 6, 101–112, doi:doi:10.5194/tc-6-101-2012, 2012.

Favier, L., Durand, G., Cornford, S., Gudmundsson, G., Gagliardini, O., Gillet-Chaulet, F., Zwinger, T., Payne, A., and Le Brocq, A.: Retreat of Pine Island Glacier controlled by marine ice-sheet instability, Nature Climate Change, 4, 117–121, doi:doi:10.1038/nclimate2094, 2014.

Gagliardini, O., Durand, G., Zwinger, T., Hindmarsh, R., and Le Meur, E.: Coupling of ice-shelf melting and buttressing is a key process in ice-sheets dynamics, Geophysical Research Letters, 37, L14 501, doi:doi:10.1029/2010GL043334, 2010.

Gagliardini, O., Zwinger, T., Gillet-Chaulet, F., Durand, G., Favier, L., de Fleurian, B., Greve, R., Malinen, M., Martín, C., Råback, P., Ruokolainen, J., Sacchettini, M., Schäfer, M., Seddik, H., and Thies, J.: Capabilities and performance of Elmer/Ice, a new-generation ice sheet model, Geoscientific Model Development, 6, 1299–1318, doi:10.5194/gmd-6-1299-2013, URL http://www.geosci-model-dev.net/6/1299/2013/, 2013.

Gudmundsson, G. H., Krug, J., Durand, G., Favier, L., and Gagliardini, O.: The stability of grounding lines on retrograde slopes, The Cryosphere, 6, 1497–1505, doi:10.5194/tc-6-1497-2012, URL http://www.the-cryosphere.net/6/1497/2012/, 2012.

Krug, J., Weiss, J., Gagliardini, O., and Durand, G.: Combining damage and fracture mechanics to model calving, The Cryosphere, 8, 2101–2117, 2014.

Pattyn, F., Schoof, C., Perichon, L., Hindmarsh, R. C. A., Bueler, E., de Fleurian, B., Durand, G., Gagliardini, O., Gladstone, R., Goldberg, D., Gudmundsson, G. H., Lee, V., Nick, F. M., Payne, A. J., Pollard, D., Rybak, O., Saito, F., and Vieli, A.: Results of the Marine Ice Sheet Model Intercomparison Project, MISMIP, The Cryosphere, 6, 573–588, doi:10.5194/tc-6-573-2012, 2012.

Pattyn, F., Perichon, L., Durand, G., L., F., Gagliardini, O., Hindmarsh, R. C. A., Zwinger, T., Albrecht, T., Cornford, S., Docquier, D., Fürst, J. J., Golberg, D., Gudmundsson, G. H., Humbert, A., Hütten, M., Huybrechts, P., Jouvet, G., Kleiner, T., Larour, E., Martin, D., Morlighem, M., Payne, A. J., Pollard, D., Rückamp, M., Rybak, O., Seroussi, H., Thoma, M., and Wilkens, N.: Grounding-line migration in plan-view marine ice-sheet models: results of the ice2sea MISMIP3d intercomparison, J. Glaciol., 59, 410–422, doi:10.3189/2013JoG12J129, 2013.